JOURNAL OF PROPULSION AND POWER
Vol. 11, No. 6, November–December 1995

Simplified Approach for Control of Rotating Stall Part 2: Experimental Results

O. O. Badmus,* S. Chowdhury,† K. M. Eveker,‡ C. N. Nett,§ and C. J. Rivera†
Georgia Institute of Technology, Atlanta, Georgia 30332

The primary objective of this article is to provide experimental validation of the simplified approach to control of rotating stall presented in Part 1 of this article. The experimental rig utilized is a low-speed, single-stage axial compressor rig. It is shown that the controller based on this approach has significant ability to reject persistent disturbances that cause the uncontrolled system to enter rotating stall. In addition, it is shown that the effective stable axisymmetric flow range of the compressor has been extended by this controller. This is a consequence of the fact that the controller enlarges the domains of attraction of linearly stable axisymmetric equilibria. A secondary objective of this article is the investigation of the presence of rotating stall precursors in this rig. Our motivation here is to determine the most appropriate signal processing to apply to sensor data prior to using it in the controller. In this rig, two first-mode rotating stall precursors traveling at different speeds are found when appropriate spectral separation of measured data is performed.

I. Introduction

THE experimental results presented in this article demonstrate both open-loop uncontrolled and closed-loop controlled behaviors pertaining to the phenomenon of rotating stall in a low-speed, single-stage axial compressor rig. Rotating stall occurs in this rig at approximately 90-Hz fundamental frequency, which is approximately one-half the rotational frequency of the compressor (177 Hz). The presence of a rotating stall precursor is investigated, and two first-mode precursors, traveling at different speeds, are found to be present in this rig when appropriate signal processing of sensed data is performed. The behavior of the system as it transitions from stable axisymmetric operation to stable nonaxisymmetric operation in rotating stall is also investigated, and it is found that the rotating stall grows smoothly out of a precursor in this rig. Experimental static bifurcation diagrams are presented for this system that illustrate the nonlinear perspective of rotating stall. It is found that hysteresis with respect to the onset and cessation of rotating stall is present in this rig. These diagrams are qualitatively in complete agreement with those discussed in Part 1 of this article.[1] The finite domains of attraction of the equilibria in this hysteresis region are evident by the jump phenomena that are present. These jump phenomena are caused by internal system noise that perturbs the system state beyond the domains of attraction of linearly stable equilibrium points, resulting in the system jumping to another linearly stable equilibrium point. Persistent disturbances are introduced to the uncontrolled system to determine their effect, so that a comparison can be made between the performance of the uncontrolled and controlled systems in the face of these disturbances. These disturbances can result in a large perturbation in the steady-state operating point of the compressor if the uncontrolled system enters rotating stall. The simplified approach for control of rotating stall presented in Part 1 is applied to the system, and closed-loop system behaviors are demonstrated. The sensors utilized by the controller consist of six static pressure sensors at the inlet of the compressor that are used to compute the first discrete Fourier transform (DFT) coefficient amplitude at each point in time. The square of this amplitude is multiplied by a gain to give a throttle perturbation that is superimposed upon the nominal throttle position. The throttle valve utilized in the controller is a one-dimensional axisymmetric effector that has an approximate small signal bandwidth of 70 Hz (about 40% of rotor frequency). Hence, it can be considered a low bandwidth actuator relative to the rotational frequency of the compressor. It is shown that the controller has significant ability to reject persistent disturbances introduced by the bleed (disturbance) valve that cause the uncontrolled system to enter rotating stall. In addition, it is shown that the effective stable axisymmetric flow range of the compressor has been extended by this controller. This is a consequence of the fact that the controller enlarges the domains of attraction of linearly stable axisymmetric equilibria. The closed-loop bifurcation diagrams of this rig are given and they are qualitatively in complete agreement with those given in Part 1 of this article.[1]

II. Experimental Facility

The experimental facility studied in this article is the LICCHUS low-speed axial compressor experimental rig in single-stage configuration,[2–5] which is shown in Fig. 1. (LICCHUS is an acronym for the Laboratory for Identification and Control of Complex Highly Uncertain Systems, School of Aerospace Engineering, Georgia Institute of Technology.) A list of the basic geometric parameters and constants of this rig is given in Table 1. The design parameters of the compressor in this rig are given in Table 2. The performance of the compressor at peak operation is given in Table 3 for a compressor speed of 10,600 rpm. The two actuators in this rig (main throttle and plenum bleed) are low inertia, high-tolerance butterfly valves and are each driven by an electric motor. They each have identical 3-dB small signal bandwidths of approximately 70 Hz.

Presented as Paper 93-2234 at the AIAA/SAE/ASME/ASEE 29th Joint Propulsion Conference, Monterey, CA, June 28–30, 1993; received May 27, 1994; revision received Jan. 25, 1995; accepted for publication Jan. 26, 1995.

*Graduate Student, School of Chemical Engineering; currently at 204, 11147-82 Avenue, Edmonton, AB T6G 0T5, Canada.

†Graduate Student, School of Aerospace Engineering; currently at 907 Beechgrove Court, Charlotte, NC 28212.

‡Air Force Laboratory Graduate Fellow, School of Aerospace Engineering; currently at United Technologies Research Center, 211 Silver Lane, M/S 129-15, East Hartford, CT 06108. Student Member AIAA.

§Associate Professor and Director, Laboratory for Identification and Control of Complex Highly Uncertain Systems (LICCHUS), School of Aerospace Engineering.

Table 1 LICCHUS axial compressor rig: geometric parameters and constants

Description	Parameter	Value
Compressor duct area	A_c	0.0046, m^2
Plenum volume	V_p	0.9220, m^3
Plenum bleed area, full open	$A_{T,36}$	0.0020, m^2
Throttle valve area, full open	$A_{T,9}$	0.0081, m^2
Rotor tip radius	r_c	0.05715, m
Compressor duct length	L_c	0.9652, m
Compressor speed	N_2	5,400–11,100 rpm
Helmholtz frequency	ω_{Helm}	3.89 Hz

Table 2 LICCHUS axial compressor rig: compressor-design parameters

Compressor design parameters	Rotor	Stator
Aspect ratio	0.272	0.332
Chord length	0.055, m	0.045, m
Stagger angle	40.6 deg	28.6 deg
Camber angle	37.2 deg	55.0 deg
Number of airfoils	7	9
Solidity	1.44	1.52
Pitch	0.0381, m	0.0297, m
Number of inlet guide vane	0	
Axial spacing	0.010, m	
Tip diameter	0.115, m	
Tip clearance, % chord length	1.39	
Hub-tip ratio	0.74	
Nominal rotor speed	10,600 rpm	

Table 3 LICCHUS axial compressor rig: compressor performance at peak operation

Compressor performance at peak operation	Value
Pressure coefficient, Ψ	0.172
Pressure ratio	1.01
Axial flow coefficient, Φ	0.368
Axial Mach number	0.0684
Tip Mach number	0.20
Reynolds number	1.84×10^5

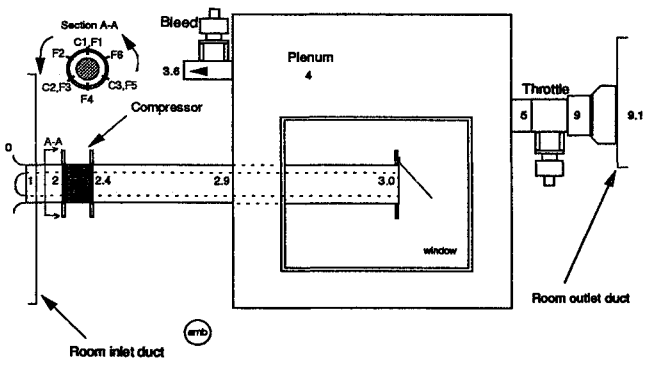

Fig. 1 LICCHUS axial compressor experimental facility.

A description of the type of sensors used on this rig and their naming convention is given in Ref. 3. The sensors that are pertinent to the work described in this article can be listed as follows: 1) six static pressure sensors (PS2F1, . . . , PS2F6) placed at equidistant locations around the circumference of the duct at the compressor inlet (station 2 in Fig. 1); 2) three circumferentially located total-static differential pressure sensors, PD2C1, . . . , PD2C3, used to compute local flow coefficient at the compressor inlet (station 2); 3) plenum static pressure sensor, PS31; 4) throttle exit static pressure sensor, PS91; 5) upstream static pressure and temperature sensors, PS0 and T0; 6) speed sensor, N2; and 7) angular position sensors for the plenum bleed and main throttle valves, THA36 and THA9, respectively.

In this article, the dimensionless variables defined in Ref. 6 are adopted for representing all flow variables. Dimensionless pressures are obtained by dividing the measured pressure signals by ρU^2, where U is the wheel tip speed, and ρ is density. The plenum pressure rise, denoted by Ψ on subsequent plots, is defined as the difference between the dimensionless plenum pressure and the upstream dimensionless total pressure. The measurement error in Ψ at peak operating conditions is $\pm 1.3\%$.[7] Flow coefficients are obtained by dividing velocities by U. The annulus-averaged flow coefficient, denoted as Φ, is obtained as the spatial average of the local flow coefficients around the circumference of the compressor. The measurement error in Φ at peak operating conditions is $\pm 0.59\%$. Dimensionless time t shown in the figures of this article is calculated by normalizing time with the time taken for one radian of wheel travel. Finally, the throttle parameter K_T is defined in this article as $K_T = \sqrt{2}A_T/A_c$, where A_c and A_T refer to the flow areas in the compressor and the throttle, respectively. In this rig, there are two throttle valves. The main throttle valve is used for control, and the plenum bleed valve takes on the role of a disturbance throttle that is used to introduce persistent disturbances to the system. A different throttle parameter is associated with each valve, $K_{C9} = \sqrt{2}A_{T,9}/A_c$ for the main (control) throttle and $K_{D36} = \sqrt{2}A_{T,36}/A_c$ for the disturbance throttle valve. In order to scale these throttle parameters in various plots given in this article, nominal values are defined. For a compressor speed of 10,600 rpm, the nominal value of the main throttle parameter $K_{C9\text{nom}}$ is 0.6297. For this setting of $K_{C9\text{nom}}$, the nominal value for $K_{D36\text{nom}}$ is 0.2563. A nonzero value for $K_{D36\text{nom}}$ is selected so that a disturbance could be introduced that throttles the system equilibrium towards stall by closing this valve. This value of $K_{D36\text{nom}}$ is selected because for the given value of $K_{C9\text{nom}}$, it is the smallest throttle parameter for the bleed valve at which rotating stall is not present in the system. Thus, when $K_{D36}/K_{D36\text{nom}} < 1.0$, the system will enter rotating stall.

III. Experimental Analysis of Rotating Disturbances

The data acquisition hardware and procedure for logging experimental data from this system are described in Ref. 3. The analysis of this data for determination of the presence of rotating disturbances is discussed in this section.

In the laboratory fixed frame (where sensors are located), a rotating disturbance such as rotating stall is an unsteady two-dimensional phenomena, i.e., it involves circumferentially and temporally varying flow properties. To analyze experimental data for such a disturbance, a flow property m (such as static pressure, mass flux, etc.), is split into an annulus average portion s, which depends only on time and a circumferentially varying portion r that has zero average around the circumference:

$$m(\theta, t) = s(t) + r(\theta, t) \quad \text{where} \quad \frac{1}{2\pi}\int_0^{2\pi} r(\theta, t)\, d\theta = 0$$

In general, we assume that r may be made up of the sum of several different wave packets:

$$r(\theta, t) = r_1(\theta, t) + r_2(\theta, t) + \cdots + r_M(\theta, t)$$

where M is the number of wave packets. We view each wave packet, r_i (where $i = 1, \ldots, M$), as a waveform with a certain mode number that is rotating around the circumference of the compressor at a speed ω_i^q. The mode number of a wave packet is determined by the number of zero crossings of the 2π periodic spatial wave, where an nth mode wave packet has $2n$ zero crossings.

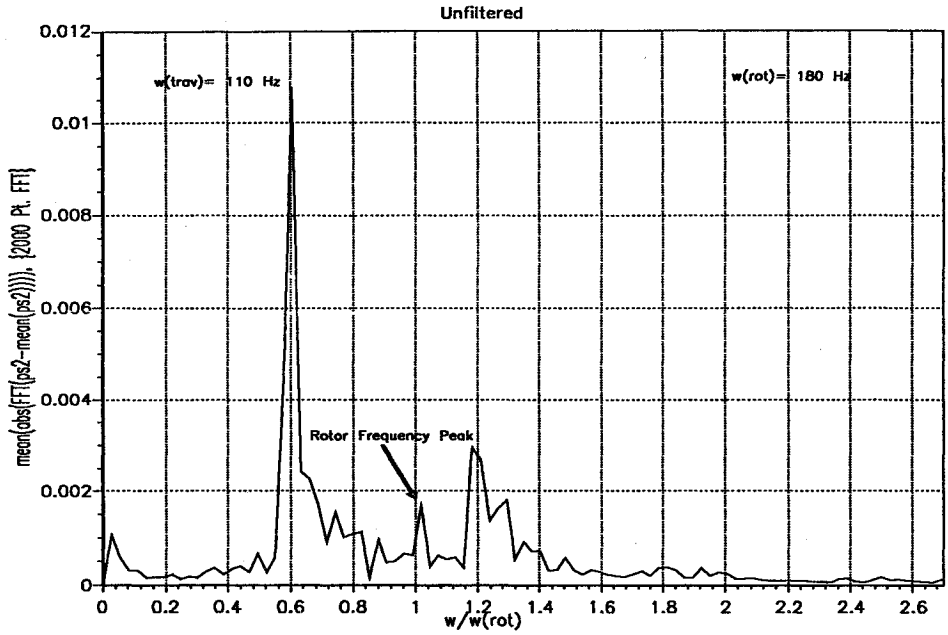

Fig. 2 Fourier transform of steady rotating stall static pressure data.

We assume that we can represent each wave packet r_i as a traveling wave that depends only on a single variable $\theta_i^d = \theta + \omega_i^d t$, in the following manner:

$$r_i(\theta, t) = d_i(\theta + \omega_i^d t) = d_i(\theta_i^d)$$

where $d_i(\cdot)$ is 2π periodic and ω_i^d is assumed to be a constant. In other words, each wave packet is assumed to be rotating at a constant speed. Since each d_i is 2π periodic in θ_i^d, we can represent it with a Fourier series expansion in terms of θ_i^d as follows[8]:

$$\begin{aligned} r_i(\theta, t) &= d_i(\theta_i^d) \\ &= \sum_{n=1}^{\infty} A_{in} \sin(n \cdot \theta_i^d + \phi_{in}) \\ &= \sum_{n=1}^{\infty} A_{in} \sin(n \cdot \theta + n\omega_i^d \cdot t + \phi_{in}) \end{aligned}$$

where A_{in} and ϕ_{in} are the magnitude and phase, respectively, of the nth harmonic of the Fourier series expansion of the wave packet r_i. Now, at a fixed θ location, the time-varying portion of the flow property r in terms of the Fourier series expansions of the wave packets r_i has the following form:

$$r_\theta(t) = \sum_{i=1}^{M} \sum_{n=1}^{\infty} A_{in} \sin[\underbrace{n\omega_i^d}_{\text{frequency}} \cdot t + \underbrace{(\phi_{in} + n \cdot \theta)}_{\text{phase}}]$$

As can be seen, there are an infinite number of components in this representation. We would like to use measured data to approximately determine the decomposition of r according to the previous relation. To accomplish this, we time-sample data at fixed θ locations at twice the frequency of the largest $n\omega_i^d$ for which A_{in} is significant, and we digitally filter the data to eliminate aliasing. Now, if we look at a fast Fourier transform (FFT) of the time sampled data at a fixed θ location, several spectral lines (seen as peaks in the FFT) will be present, which will correspond to the important frequencies ($n\omega_i^d$) present in the previous representation of r. To determine what wave packets contribute to each spectral line, the rotational speeds of these wave packets, and the harmonic contents of these wave packets, each line must first be isolated using identical bandpass filtering on all sensors located at several different θ locations. Once this has been done, the only terms left in the previous representation will correspond to the same values of $n\omega_i^d$. Next, looking at the representation of r at a given time t, we see that

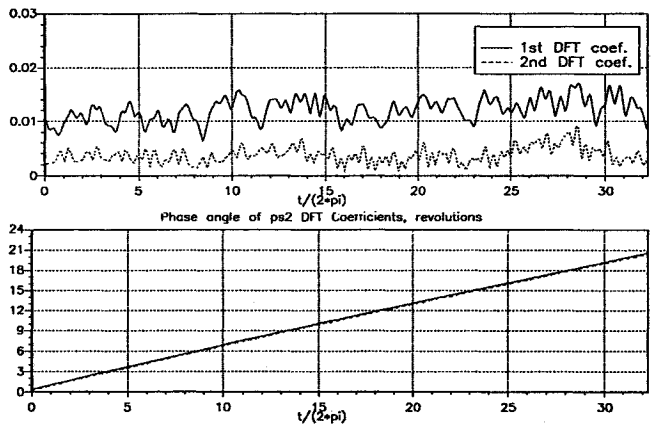

Fig. 3 Magnitude and phase angle of static pressure DFT coefficients.

$$r_i(\theta) = \sum_{i=1}^{M} \sum_{n=1}^{\infty} A_{in} \sin[\underbrace{n}_{\text{frequency}} \theta + \underbrace{(\phi_{in} + n\omega_i^d \cdot t)}_{\text{phase}}]$$

If we perform a DFT computation on the spatial data once they have been bandpass filtered, we can determine the spatial frequencies of the waves that are present in this spectral line, along with their rotational speeds. To perform the DFT computations, the θ sampling must be at a rate greater than $2N$ (i.e., at least $2N + 1$) to avoid aliasing, where N is the highest mode number with significant A_{in} in the earlier representation. There can only be a single wave present at each spatial frequency n, since all other waves of the same n traveling at different speeds have been eliminated by the bandpass filtering. This is important because the DFT computation will only have to approximate a single wave of n, and the phase variation of the nth DFT coefficient will be linear as a function of time. In this case, there is no ambiguity as to whether a harmonic of a wave packet with this particular n rotating at a speed of ω_i^d is present.

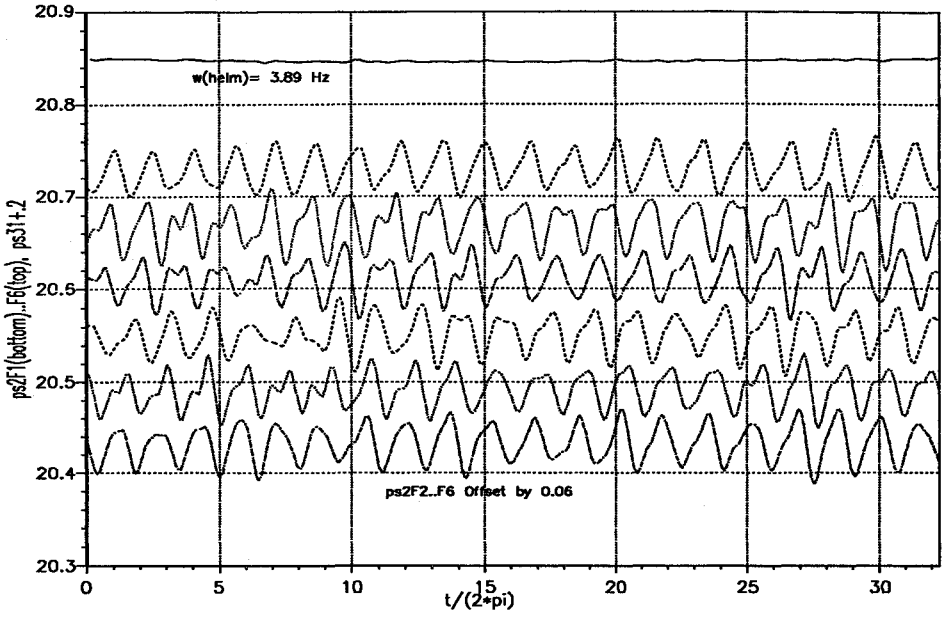

Fig. 4 Steady rotating stall static pressure data at six circumferential positions.

If there were more than one wave with n present in the data traveling at different speeds, the DFT computation would try to approximate both waves with the nth DFT coefficient resulting in the phase not varying linearly with time. As an example, consider the case of the following two-wave packet disturbance:

$$r(\theta, t) = A_{11} \sin(\theta - \omega_1^d t) + A_{21} \sin(\theta - \omega_2^d t)$$

where each wave packet has a mode number of $n = 1$. The amplitude of the first Fourier series coefficient of this wave can be computed as

$$A^2 = A_{11}^2 + A_{21}^2 + 2A_{11}A_{21} \cos[(\omega_1^d - \omega_2^d)t]$$

and the phase angle can be computed as

$$\phi = -\tan^{-1}\left(\frac{A_{11} \sin \omega_1^d t + A_{21} \sin \omega_2^d t}{A_{11} \cos \omega_1^d t + A_{21} \cos \omega_2^d t}\right)$$

As can be seen, the amplitude is sinusoidal, and the phase angle does not increase at a linear rate. Now, if the signal had been bandpass filtered to isolate the frequency ω_1^d, the resulting amplitude would be

$$A^2 = A_{11}^2$$

and the phase angle would be

$$\phi = \omega_1^d t$$

and so the amplitude will be constant and the phase angle will vary linearly. Thus, there is no ambiguity regarding the presence of a wave packet that contains a harmonic with spatial frequency $n = 1$ traveling at a speed of ω_1^d.

In summary, to determine the components that make up r, each peak in the FFT of time sampled data from a single sensor (corresponding to components of r that have a particular value of $n\omega_1^d$) must be isolated by bandpass filtering all sensor measurements. Then, a DFT of the filtered spatial measurements is performed to see what spatial frequencies n are present and what their rotational speeds are, as indicated by DFT coefficients with linear phase variation. Once all of the spectral lines have been investigated, all harmonics of the different waves packets present in the disturbance will have been determined and the wave packets can be examined to determine their mode number.

In Fig. 2, the FFT of experimental data from a static pressure sensor at the compressor inlet is given for the system operating in rotating stall. As can be seen, there are only two prominent peaks, one at approximately 110 Hz ($\omega/\omega_{rot} = 0.62$) and one at approximately 220 Hz ($\omega/\omega_{rot} = 1.24$). Since there are only two peaks, we do not isolate them using the bandpass filtering before doing the DFT computation. If the phase angles of the DFT coefficients do not vary linearly, however, we will have to redo the computation after first isolating the peaks using bandpass filters on the individual signals. The magnitude and phase of the first and second DFT coefficients computed using rotating stall data taken from the six equally spaced sensors around the circumference of the compressor are shown in Fig. 3. As can be seen, the magnitudes are approximately constant (although somewhat noisy) and the phase angles are increasing linearly at the same rate. Thus, the two peaks correspond to the first and second harmonics of a wave packet traveling at 110 Hz. This wave packet corresponds to fully developed rotating stall. Note that higher order harmonics of this disturbance may be present, but they may not appear due to sensor bandwidth limitations. Since the first harmonic has a significantly higher magnitude than the second harmonic, the rotating stall is a first mode wave (only two zero crossings). This is further illustrated in Fig. 4, which shows the time traces of the six sensors that indicate a 110-Hz oscillation in the six sensors with a 60-deg phase shift between them. Analysis of this disturbance was simplified because only a single significant wave packet is present and isolation of spectral lines was not required. However, when more than one wave packet is present in a disturbance, the technique previously described must be utilized. This is demonstrated in the sequel.

IV. Open-Loop System Behavior

In this section, various open-loop uncontrolled behaviors of the system are demonstrated.

A. Stall Precursor

In previous experimental studies, the existence of stall precursors in various low-speed axial compressors has been established. It is shown[9,10] that small-amplitude modal perturbations that grow smoothly into rotating stall are present in the compressor. In Ref. 11 similar results were also given.

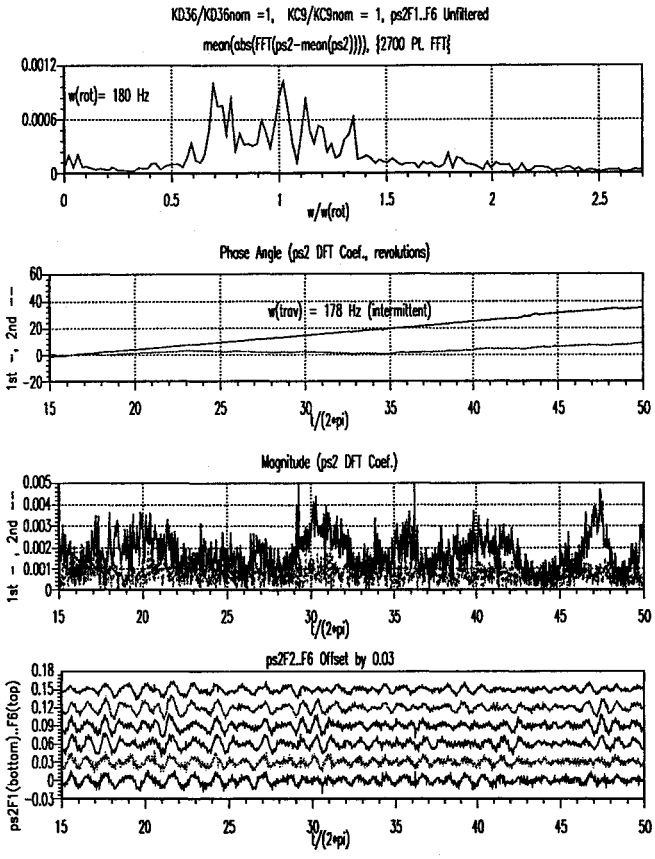

Fig. 5 Stall precursor data at $K_{D36}/K_{D36nom} = 1.0$ unfiltered.

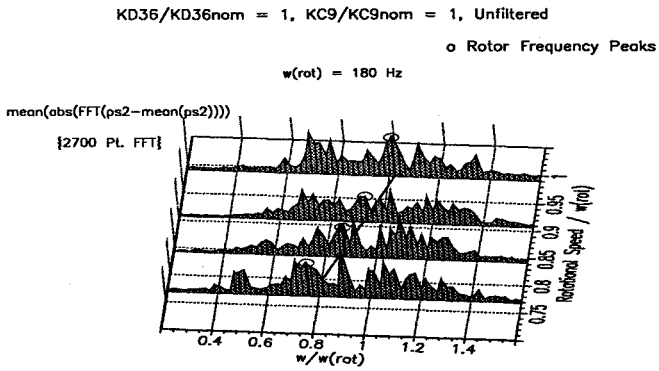

Fig. 6 Rotor frequency FFT peaks for various compressor speeds.

However, it was also shown[11] that in some configurations small short-length scale perturbations could initiate rotating stall. For these cases, the rotating stall did not grow smoothly out of modal perturbations in the compressor. To determine what type of, if any, rotating stall precursor is present in the rig studied in this article, data was taken in the stable region of compressor operation close to the stall point.

In Fig. 5, the FFT of unfiltered static pressure sensor data from a single θ location at the compressor inlet is shown along with time traces and the DFT of unfiltered static pressure sensor data from six circumferential locations at the compressor inlet. This data corresponds to operation at a disturbance throttle position of $K_{D36}/K_{D36nom} = 1.0$ for the nominal compressor rotational speed of 10,600 rpm. The FFT plot indicates that there are several spectral lines with significant amplitude. Since the data is unfiltered, multiple waves with the same spatial frequency must be approximated by the DFT. Hence, the phase of the DFT coefficients will not vary linearly, as is seen in Fig. 5. There are other wave packets present, besides the ones of interest, which should be taken into account when isolating the wave packets of interest. These include 1) a stationary wave packet due to constant offsets between the various sensor measurements because of calibration errors, 2) wave packets corresponding to hf noise, and 3) a wave packet traveling at the rotor speed due to the plane of the rotor not being exactly perpendicular to the shaft axis. With regard to the latter, in Fig. 5 there is a peak in the FFT at the compressor rotational frequency. To verify that this peak could be attributed to a disturbance created by the rotor, the FFT for data taken at several speeds is shown in Fig. 6, which indicates a prominent peak at the rotor frequency for all speeds. Therefore, the data must be bandpass filtered to remove effects caused by the dc offsets and hf noise and bandstop filtered to remove the disturbance at the compressor rotational frequency. If we would attempt to use the

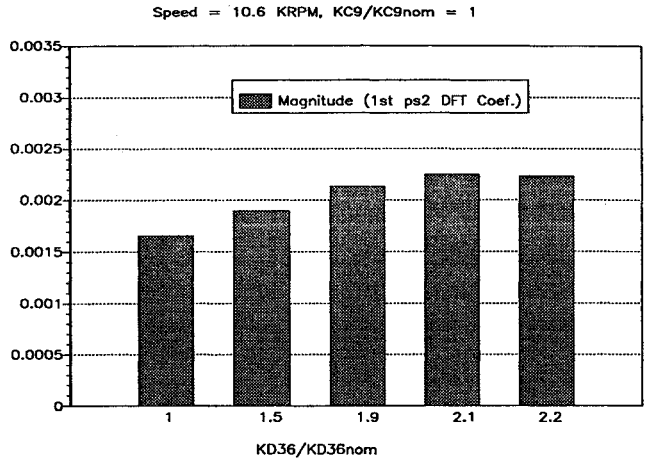

Fig. 7 Magnitude of first ps2 DFT coefficients for unfiltered data for various throttle settings.

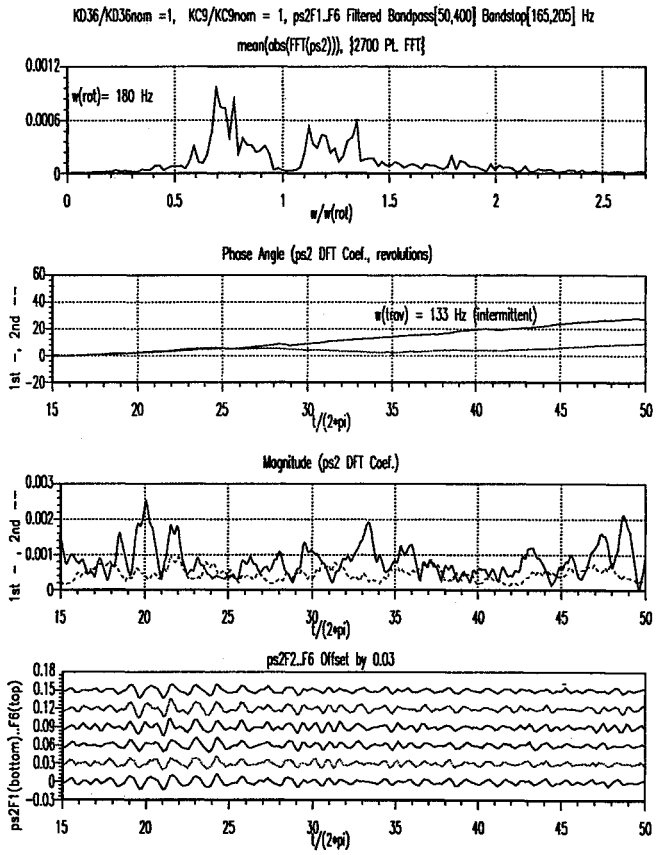

Fig. 8 Stall precursor data at $K_{D36}/K_{D36nom} = 1.0$ with bandpass and bandstop filters.

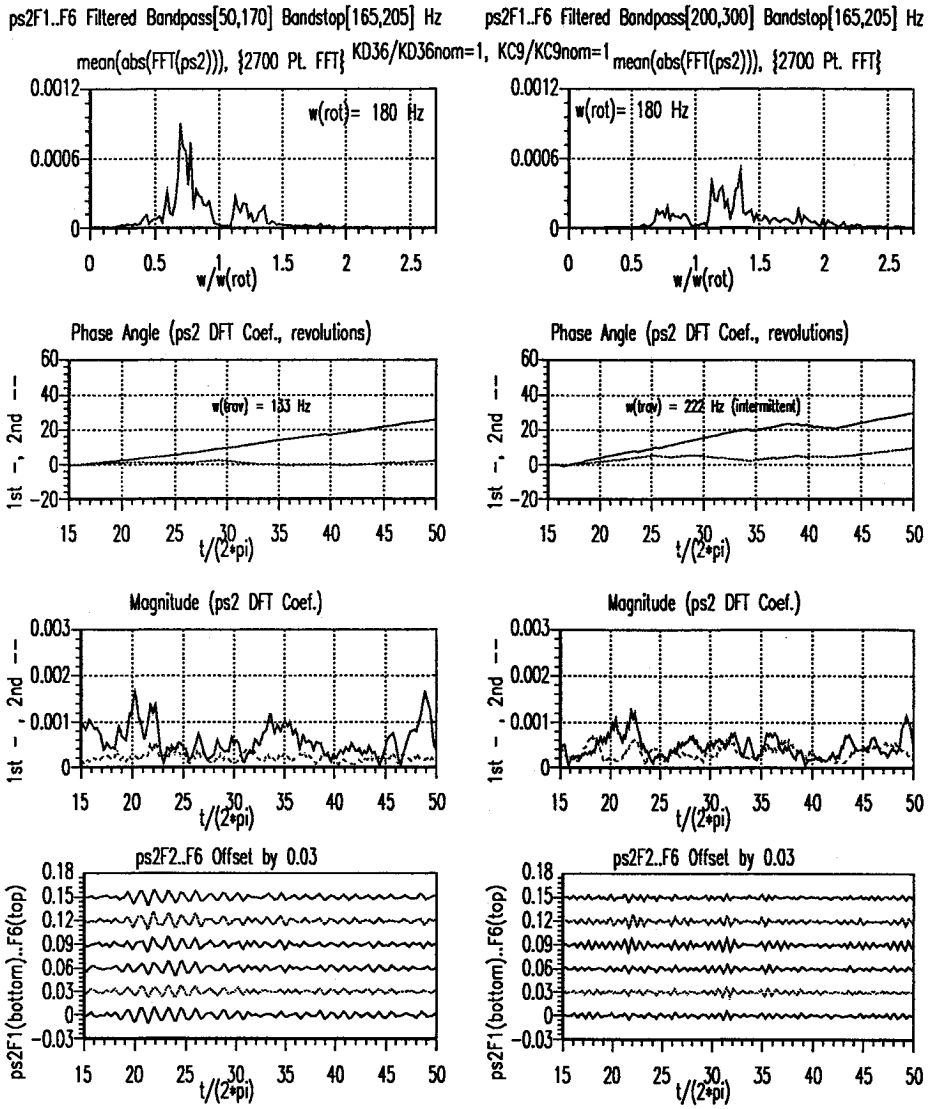

Fig. 9 Stall precursor data at $K_{D36}/K_{D36\text{nom}} = 1.0$ with bandpass filters for two frequency ranges.

magnitude of the first DFT coefficient computed using unfiltered data as a rotating stall precursor, Fig. 7 indicates that the candidate precursor magnitude will decrease (instead of increase) as a disturbance throttles the system towards rotating stall. Appropriate digital filtering of measured data is required before the DFT computation is performed to determine if a precursor is present.

The plots shown in Fig. 8 are obtained by filtering the same measured data shown in Fig. 5 with a [50,400]-Hz digital bandpass filter and [165,205]-Hz digital bandstop filter before FFT and DFT computations are performed. In the FFT, there appears to be two prominent peaks that could correspond to precursor waves. The first DFT coefficient computed from the data when filtered in this manner indicates that there may perhaps be a precursor wave rotating at 133 Hz around the compressor. However, the linear phase variation is intermittent. Thus, the peaks must be isolated before DFT computations are performed. The filters selected are [50,170]- and [200,300]-Hz bandpass filters for the lf and hf peaks, respectively. Figure 9 shows the results of FFT and DFT computations when measured data is filtered in these two different manners. When the measured data is filtered with the [50,170]-Hz bandpass filter, the phase angle of the first DFT coefficient varies linearly. Hence, there is a wave packet with spatial frequency $n = 1$ traveling at about 133 Hz. When the measured data is filtered with the [200,300]-Hz bandpass filter, the phase angle of the first DFT coefficient varies linearly (although intermittently at one point). Hence, there is a different wave packet with spatial frequency $n = 1$ traveling at 222 Hz. Since only the first harmonic of each of these wave packets was found, they are both considered first mode wave packets. It appears then that there are two first mode disturbances traveling around the circumference of the compressor at different speeds that could both be interpreted as rotating stall precursors.

When the disturbance throttle is closed slightly to a point for which $K_{D36}/K_{D36\text{nom}} < 1.0$, rotating stall appears. This behavior is shown in Fig. 10. In this figure, the three different filtering schemes utilized earlier are once again used to filter measured data before DFT computations are performed. The first set of plots correspond to the measured data being filtered with the [50,400]-Hz bandpass filter. When the system enters rotating stall, a 110-Hz oscillation appears in the static pressure sensors at station 2, the plenum pressure rise Ψ drops, the magnitudes of the first and second DFT coefficients increase above noise level, and the phase of the first and second DFT coefficients increase linearly at a rate of 110 Hz. Since the first harmonic has significantly higher magnitude than the second harmonic, the rotating stall is a first mode traveling wave. This is also seen in the time trace plots. The phase angle plots show intermittent linear phase variation before rotating stall is present, this is expected since this filtering scheme does not properly isolate the rotating stall precursor wave present in this region. The next two sets of plots cor-

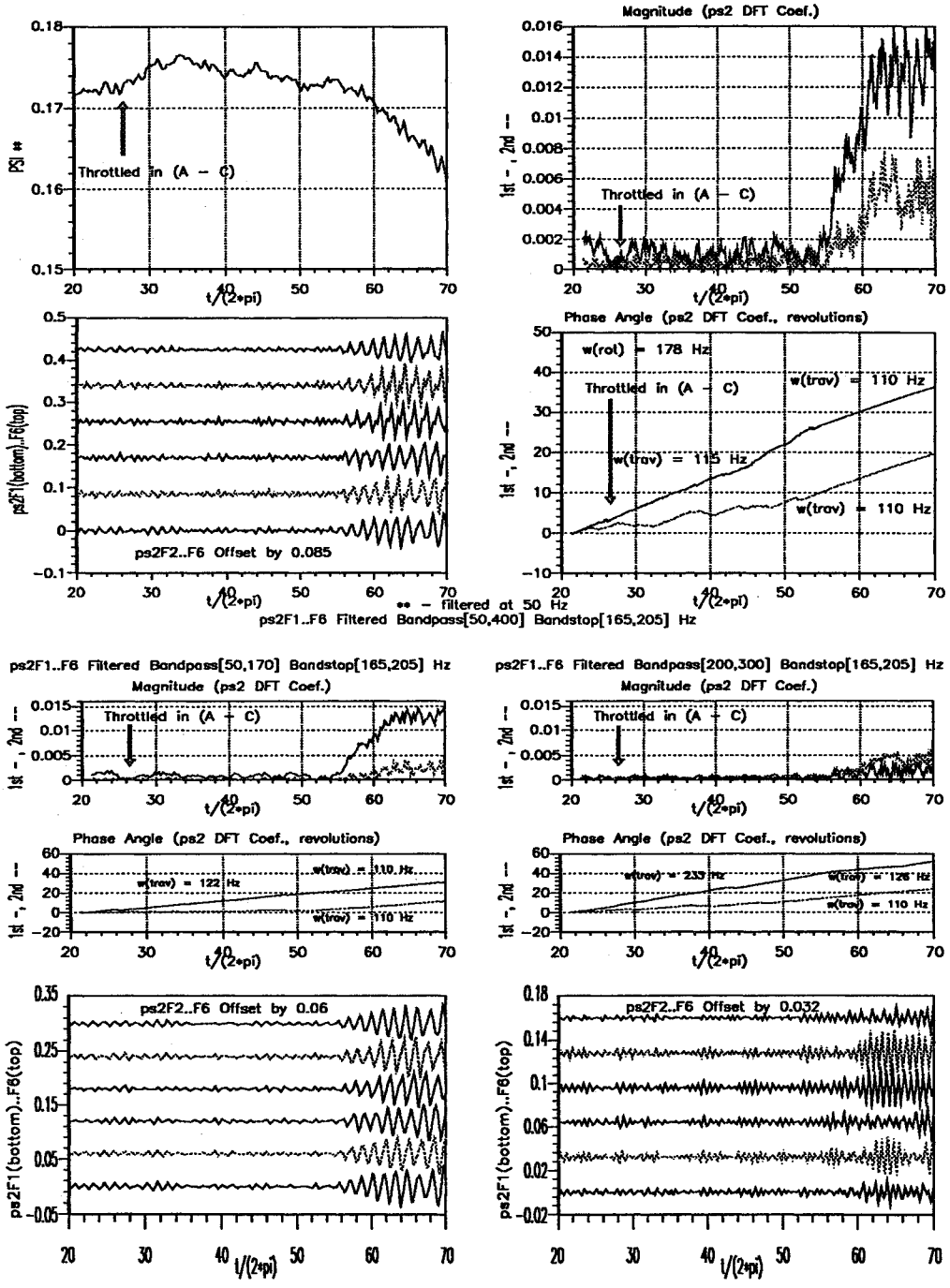

Fig. 10 Rotating stall inception.

respond to the measured data being filtered with [50,170]- and [200,300]-Hz bandpass filters, respectively, before DFT computations are performed. When the measured data is filtered with the [50,170]-Hz filter, a 122-Hz first-mode rotating stall precursor wave is seen to be present with nonintermittent linear phase variation. This precursor is seen to grow smoothly into the 110-Hz first-mode rotating stall traveling wave. When the measured data is filtered with the [200,300]-Hz filter, a first-mode precursor wave traveling at 233 Hz is present before rotating stall, although the linear phase variation seems to be somewhat intermittent. When rotating stall appears, this precursor wave gradually becomes masked by the second harmonic of the rotating stall wave traveling at 110 Hz.

Since the first-mode precursor wave traveling at 122 Hz is seen to grow smoothly into rotating stall and has consistent nonintermittent linear phase variation, it appears to be the best candidate for indication of impending rotating stall. Of course, as has been pointed out, proper filtering is required in order to observe this precursor. When data is taken at various throttle positions and at different compressor speeds (see Fig. 11), it is seen that the magnitude of this precursor wave does in fact give a good indication of impending rotating stall. This magnitude increases as the disturbance throttles the system towards rotating stall. By determining the most appropriate filtering technique for observing this rotating stall precursor, we have also determined the best filtering technique for use in the feedback controller discussed later in this article. In this controller, the amplitude of the first ps2 DFT coefficient (computed from the inlet static pressure sensors, PS2F1 . . . F6) of the rotating stall wave is used for feedback. Since the 122-Hz rotating stall precursor wave grows smoothly into rotating stall, the filtering scheme determined previously

for detection of this precursor should be used in the control scheme to ensure that the correct amplitude is computed by the controller.

B. Bifurcation Diagram

In this section, the nonlinear behavior of the axial compressor rig is discussed by giving the experimentally measured open-loop uncontrolled bifurcation diagram. The experimental bifurcation diagram near the peak of the pressure rise characteristic for a compressor speed of 10,600 rpm is shown in Fig. 12. Data for this diagram is obtained by varying the disturbance throttle valve in the finest steps possible and making measurements when the system reaches steady-state operation. In this figure, for high values of disturbance throttle position, there is a single linearly stable axisymmetric equilibrium point for which rotating stall is not present. These points are indicated by a $+$. For low values of disturbance throttle position, there is a single linearly stable nonaxisymmetric equilibrium point that corresponds to rotating stall. These points are indicated by a $\times$. At certain values of throttle position, there exist two stable equilibria, one axisymmetric ($+$) and one nonaxisymmetric ($\times$). These points are circled and connected with dash–dot lines to indicate that the system jumps between these two equilibrium points at that position of the disturbance throttle. The jumps occur naturally in the system due to impulsive disturbances that perturb the system state beyond the finite domains of attraction of these linearly stable equilibria. The existence of multiple equilibria for a given throttle setting indicates the presence of a small region of hysteresis with respect to the onset and cessation of rotating stall in this rig. Notice the abrupt change in the steady-state rotating stall amplitude as the disturbance throttle is varied

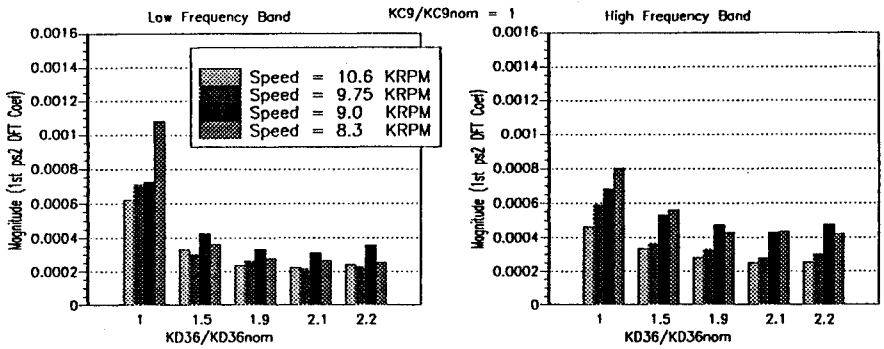

Fig. 11 Stall precursors.

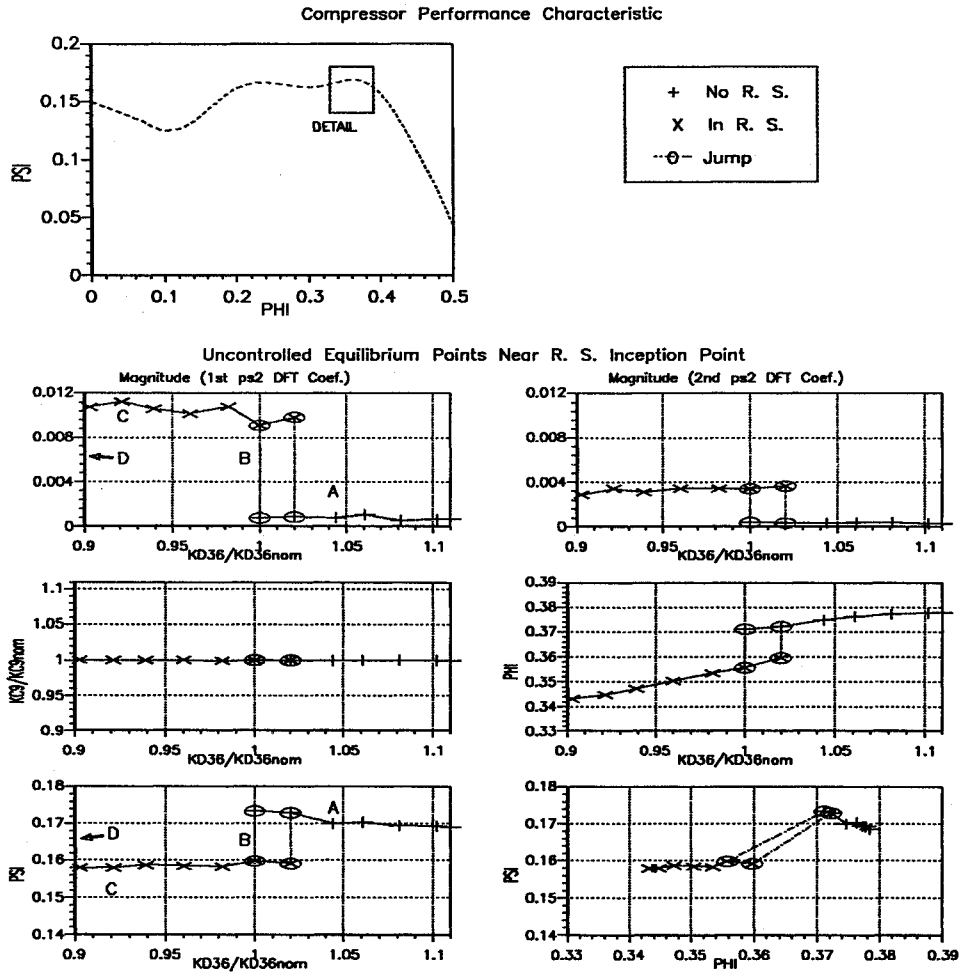

Fig. 12 Uncontrolled experimental bifurcation diagram.

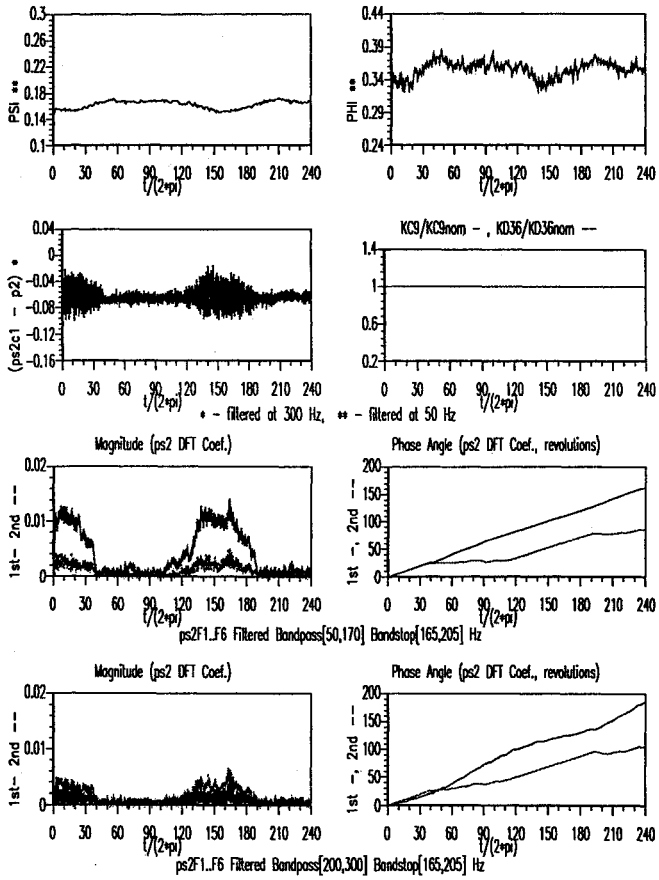

Fig. 13 Uncontrolled operation at point B.

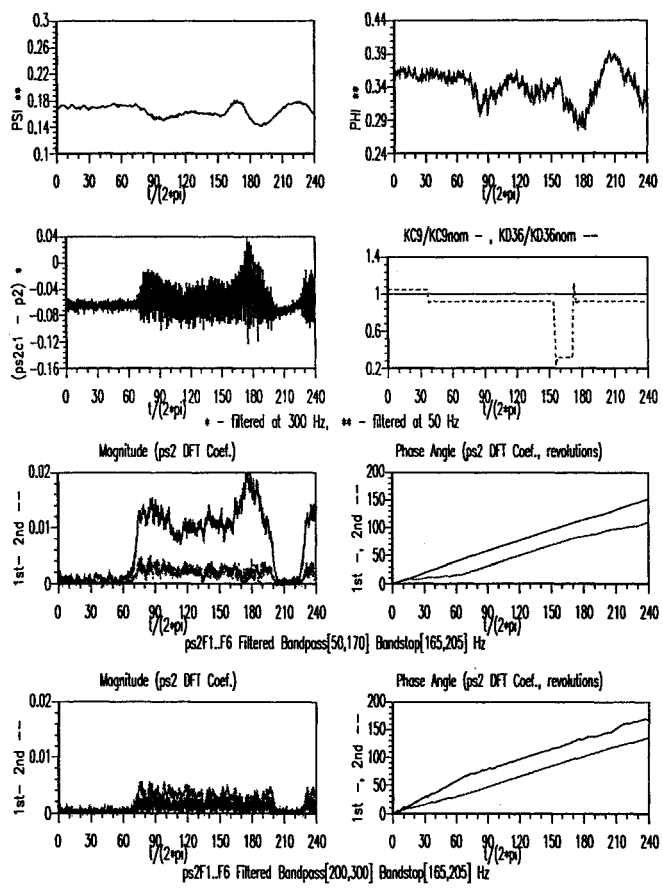

Fig. 14 Uncontrolled transition into rotating stall (A—C—transient—C).

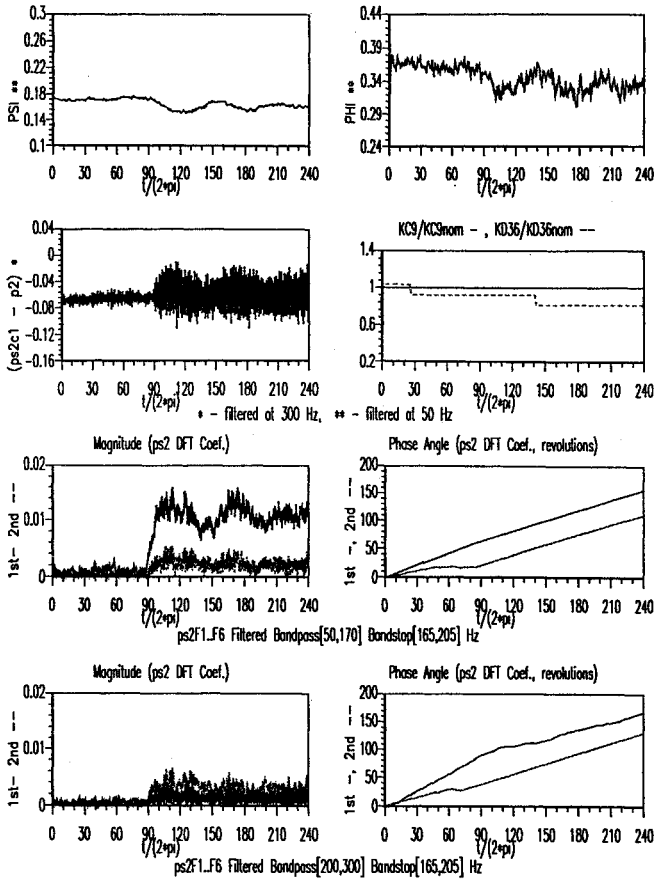

Fig. 15 Uncontrolled transition into rotating stall (A—C—D).

and the system enters rotating stall. This results in an abrupt change in the operating point of the compressor, as seen on the compressor performance map. The behaviors depicted here in the experimental bifurcation diagrams of this system are qualitatively completely consistent with the behaviors discussed in Part 1 of this article.[1]

There are several points labeled in this diagram that will be referred to in the sequel. Point A corresponds to a disturbance throttle position at which there is only a single stable axisymmetric equilibrium point. Point B corresponds to a disturbance throttle position at which the system jumps between two linearly stable equilibrium points, one axisymmetric and one nonaxisymmetric. Point C corresponds to a disturbance throttle position at which there is a single stable nonaxisymmetric equilibrium point. Finally, point D corresponds to a disturbance throttle position less than that of point C at which there is once again a single stable nonaxisymmetric equilibrium point.

Figure 13 shows transient data with the disturbance throttle positioned at point B for which the system jumps between the stalled and unstalled equilibrium points. The small domains of attraction of these linearly stable equilibrium points can be assessed by observing that the system jumps between these equilibrium points without any variation of the disturbance throttle. At one instant, the system is in rotating stall, but suddenly recovers (moves to axisymmetric equilibrium) for a short period of time. The system then drops back to the rotating stall equilibrium. The internal system noise provides a large enough impulsive disturbance to perturb the system state beyond the domains of attraction of both of these linearly stable equilibrium points.

C. Forced Transients

In this section, some persistent disturbances are introduced with the disturbance throttle to demonstrate their effect on

the uncontrolled system. Later, the effect of the same persistent disturbances on the controlled system are demonstrated and compared to the behaviors demonstrated here.

Two sequential disturbance scenarios are introduced to the system in the plots of Fig. 14. The first is a change in disturbance throttle position from point A to point C, while the second is a pulse change at point C. In the first scenario of Fig. 14, the system starts in stable axisymmetric operation with the disturbance throttle set at point A. The disturbance throttle is then moved to point C to introduce a persistent disturbance to the system. Shortly after the persistent disturbance is introduced to the system, rotating stall develops. As can be seen, an abrupt change in steady-state rotating stall amplitude occurs as a result of this disturbance acting on the system. This results in an abrupt change in the steady-state operating point of the compressor, as is evidenced by the reduced annulus-averaged flow coefficient Φ and annulus-averaged pressure rise Ψ after the disturbance occurs.

In the second scenario of Fig. 14, a large impulsive disturbance is introduced to the system (using the disturbance throttle valve). This is done by moving the disturbance throttle to a different point for a very short period of time and then returning it to point C, thereby establishing a large perturbation of the system state from the equilibrium point. After the system state is perturbed from the equilibrium point by the large impulsive disturbance, the system returns to stable non-axisymmetric operation at point C. During this transient, the rotating stall momentarily goes away. However, since the linearly stable nonaxisymmetric equilibrium point C is a global attractor, the system returns to point C after the impulsive disturbance.

In the scenario of Fig. 15, the system once again starts in stable axisymmetric operation at point A. The disturbance throttle is then moved to point C to introduce a persistent disturbance to the system. Shortly thereafter, the disturbance throttle is moved to point D to introduce a second persistent disturbance to the system. As can be seen in Fig. 15, rotating stall develops shortly after the first persistent disturbance acts on the system. After the second persistent disturbance acts on the system, the rotating stall is still present, and an even larger change in the steady-state operating point of the compressor occurs, as compared to that of the previous scenario.

V. Closed-Loop System Behavior

In this section, the simplified approach to control of rotating stall discussed in Part 1 is implemented on the rig considered in this article. Figure 16 shows the block diagram of this controller as implemented on this rig. Data from six static pressure sensors at the face of the compressor is sampled at

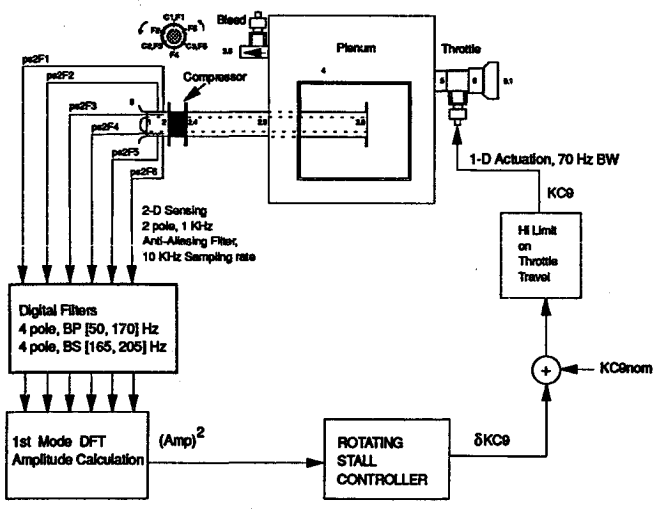

Fig. 16 Rotating stall controller diagram.

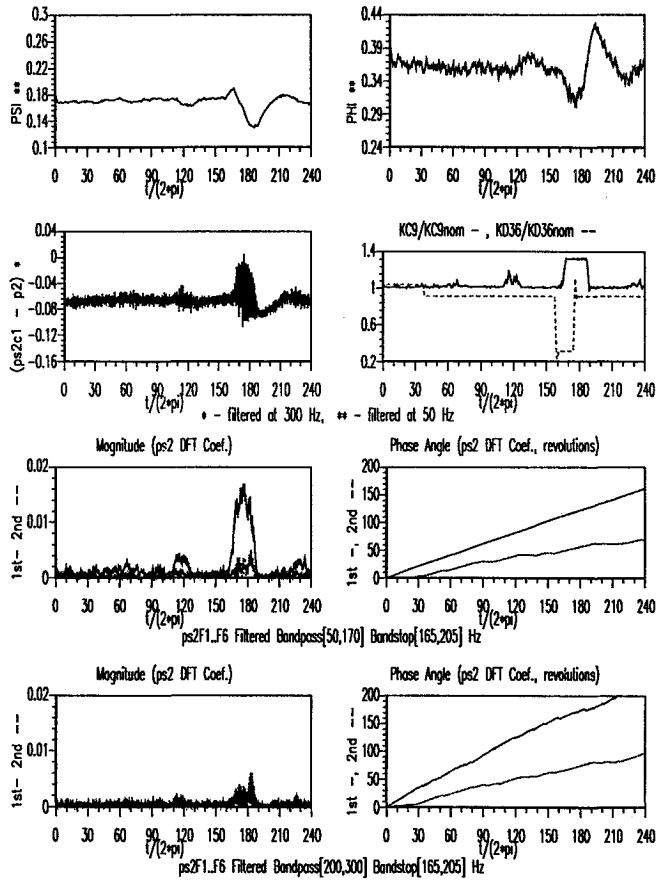

Fig. 17 Rotating stall controlled (A—C—transient—C).

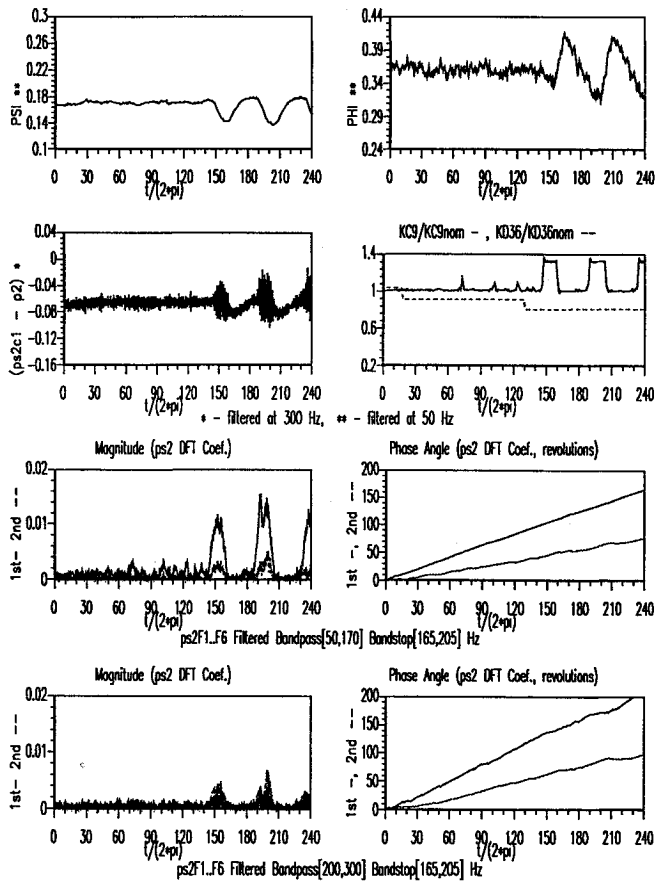

Fig. 18 Rotating stall controlled (A—C—D).

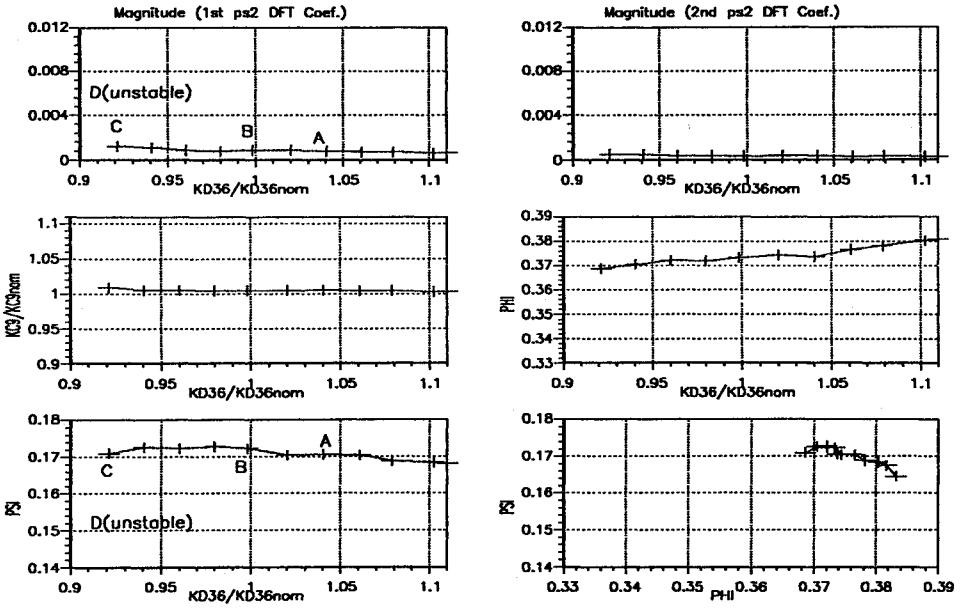

Fig. 19 Rotating stall controlled bifurcation diagram.

a rate of 10 KHz and is processed by 1 KHz antialiasing filters followed by a [50,170]-Hz bandpass digital filter combined with a [165,205]-Hz bandstop digital filter. As mentioned earlier, this filtering scheme is required in order to detect a rotating stall precursor wave by computing the magnitude of the first ps2 DFT coefficient. In this controller, the amplitude of the first ps2 DFT coefficient of the rotating stall wave is used for feedback. Since the rotating stall precursor wave grows smoothly into rotating stall, the filtering scheme determined for detection of the rotating stall precursor is used in the controller to ensure that the correct amplitude (Amp) is computed. The control perturbation is computed as $k(\text{Amp})^2$, where k is an adjustable controller gain, and it is added to the nominal main throttle position $K_{C9\text{nom}}$. This control structure is the same as that discussed in Part 1 of this article,[1] except that the amplitude utilized here is computed using static pressure measurements instead of flow measurements. A maximum limit is set on the demanded throttle position in this controller in order to limit the travel of the main throttle. The control output is sent to the actuator at a rate of 10 KHz. Note that the actuator bandwidth in this system is 70 Hz, which is less than the frequency of the rotating stall (110 Hz) and significantly less than the rotational frequency of the compressor (180 Hz). The actuator bandwidth required by this controller is relatively low compared to that required by controllers that act upon the phase of the rotating stall traveling wave.[12-16]

In order to establish the controlled system performance, the system is subjected to an identical sequence of disturbance scenarios as in Fig. 14. The controlled system response to these disturbance scenarios are shown in the plots of Fig. 17. In the first scenario of Fig. 17, the system starts in stable axisymmetric operation at point A with the controller on. As can be seen, after the persistent disturbance is introduced to the controlled system, rotating stall does not develop. The controller has succeeded in rejecting this persistent disturbance and stable axisymmetric operation is maintained. Note that relatively little control action is required and that the limit on the actuator travel is not reached. Of course, since the system does not enter rotating stall, no abrupt change in the steady-state operating point of the compressor occurs.

In the second scenario of Fig. 17, a large impulsive disturbance is introduced to the system (using the disturbance throttle valve). This is done by moving the disturbance throttle to a different point for a very short period of time and then

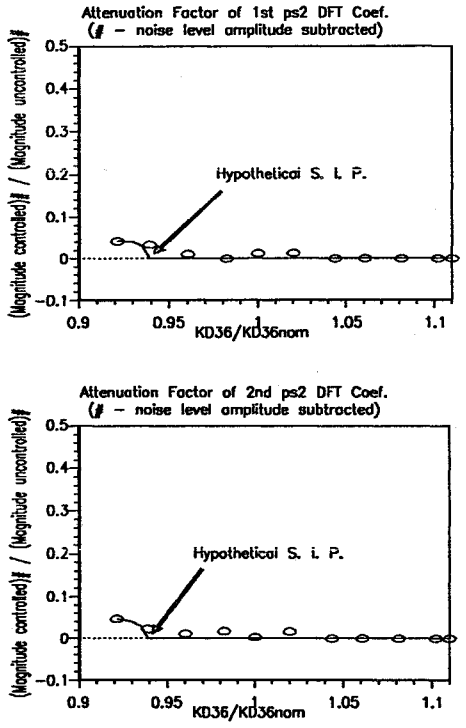

Fig. 20 Disturbance rejection in controlled system.

returning it to point C, thereby establishing a large perturbation of the system state from the equilibrium point. When the large impulsive disturbance acts on the system to create a perturbation of the system state from the equilibrium point, the system still returns to stable operation. This demonstrates the large domain of attraction of the stable equilibrium point C in the controlled system. During the transient in which the system returns to the equilibrium point, the system temporarily enters rotating stall. However, this may be due to the fact that the limit on actuator travel is reached temporarily when the impulsive disturbance was introduced to the system. Nonetheless, the system still returned to stable operation, which is the desired result. Once again, no abrupt change in the steady-state operating point of the compressor occurs in this scenario.

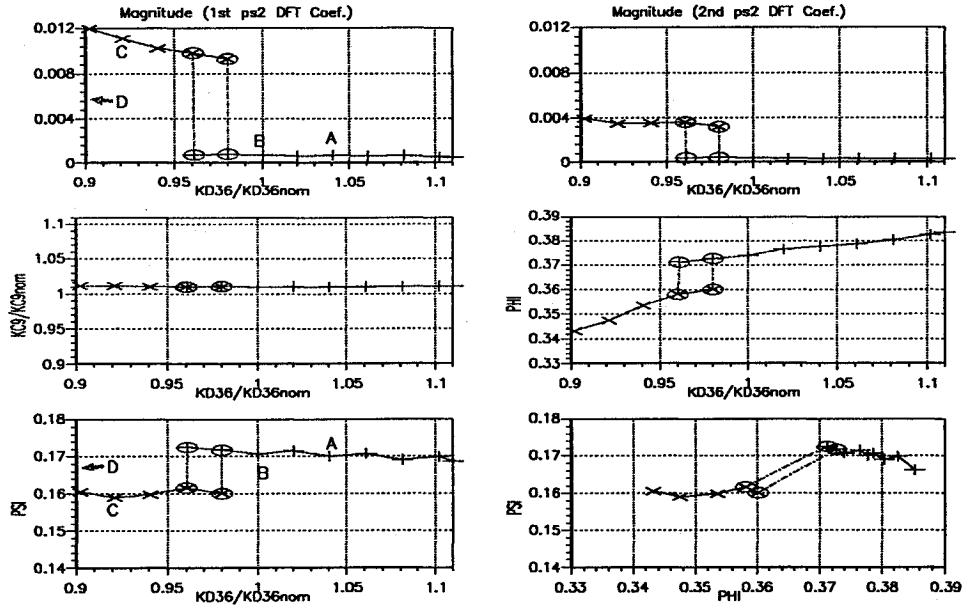

Fig. 21 Uncontrolled bifurcation diagram with offset in K_{C9}.

In Fig. 18, the system starts in stable axisymmetric operation at point A with the controller on. The same disturbance scenario as that used in Fig. 15 is utilized here. First, the disturbance throttle is moved to point C to introduce a persistent disturbance to the system. Shortly thereafter, the disturbance throttle is moved to point D to introduce a second persistent disturbance to the system. As can be seen, the controller has succeeded in rejecting the first persistent disturbance and stable axisymmetric operation is achieved. However, when the second persistent disturbance is introduced, the controller can no longer eliminate rotating stall and a controller-induced limit cycle develops in the system. This limit cycle can be partially attributed to hard nonlinearities that exist in the system due to actuator limitations. In addition, the controller utilized here was tuned experimentally, and the existence of this limit cycle suggests that the controller parameters are not optimal. Moreover, once a quantitatively accurate model of this rig is obtained, this limit cycle can potentially be eliminated via analytical control design. Thus, the presence of this limit cycle should not, at this point in time, be viewed as a fundamental limitation of this approach.

The experimentally determined bifurcation diagram of the controlled system is given in Fig. 19. Data for this diagram was obtained from the controlled system by varying the disturbance throttle valve in the finest steps possible and taking measurements when the system reaches steady-state operation. In this figure, for all values of disturbance throttle position, there is a single linearly stable axisymmetric equilibrium point. For disturbance throttle positions less than the minimum for which data is shown on this plot, the system enters the controller-induced limit cycle demonstrated in Fig. 18. The persistent disturbances that caused rotating stall in the uncontrolled system have been rejected by this controller. The disturbance rejection achieved by the controller is clearly evident by comparing the values of A for the same K_{D36} in both the controlled and uncontrolled system. In Fig. 20, a plot of an attenuation factor $(\text{Amp})_{\text{controlled}}/(\text{Amp})_{\text{uncontrolled}}$ as a function of $K_{D36}/K_{D36\text{nom}}$ is given for the first and second ps2 DFT coefficients. The noise level amplitude has been subtracted in computing the attenuation factor. Also, for purposes of this plot, the ratio of 0/0 when it occurs is set equal to 0. This plot indicates that the rotating stall amplitude is either completely eliminated or significantly reduced by the controller. Since in the uncontrolled system experimental bifurcation diagram in Fig. 12, rotating stall first appears (in the form of jump phenomena) at $K_{D36}/K_{D36\text{nom}} = 1.02$, this plot indicates that there is significant extension of the range of disturbances of this type that can be tolerated without the system entering rotating stall. The hysteresis with respect to the onset and cessation of rotating stall has been eliminated. In addition, the abrupt change in the steady-state operating point of the compressor no longer occurs. The effects of impulsive disturbances are also attenuated since the stable axi-

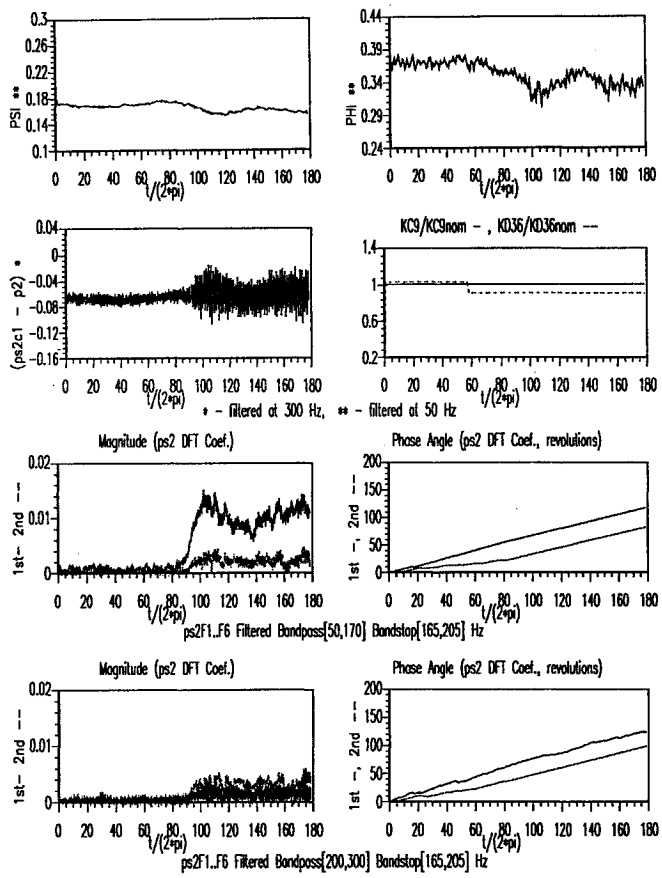

Fig. 22 Uncontrolled transition into rotating stall (A—C) with offset in K_{C9}.

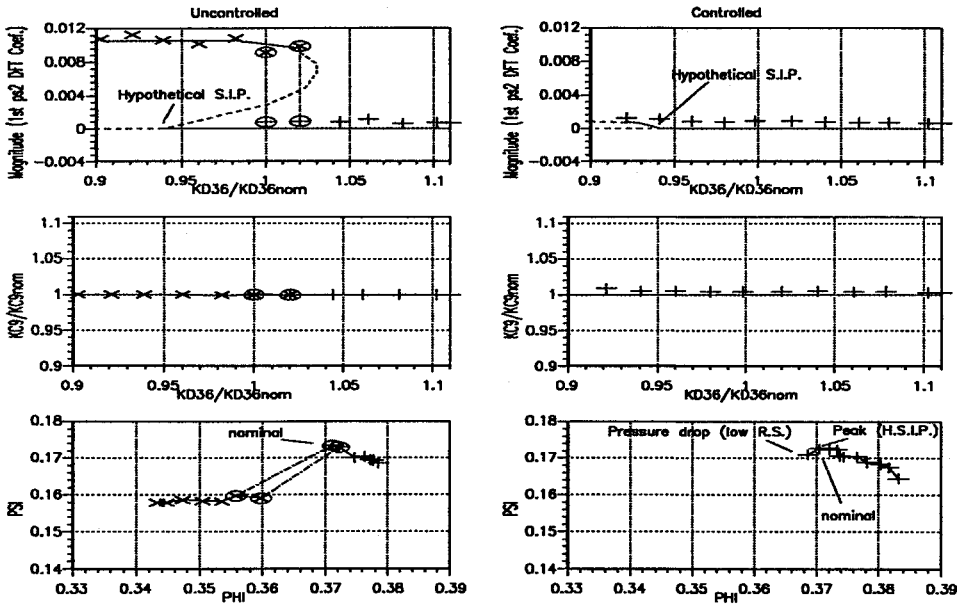

Fig. 23 Hypothetical bifurcation diagram.

symmetric equilibria are global attractors in the controlled system. This is evidenced by the lack of the jump phenomena that occur in the uncontrolled case. The experimental behaviors shown earlier for the controlled system are qualitatively in complete agreement with the behaviors discussed in Part 1 of this article.[1]

As depicted in Fig. 19, there is a slight time-averaged offset in K_{C9} induced by the controller due to noise. To show that the system has indeed been controlled instead of just being throttled into a region of previously stable operation, the uncontrolled bifurcation diagram was measured once again with the maximum offset in Fig. 19 added to K_{C9}. This bifurcation diagram is shown in Fig. 21, and was obtained in the same manner as the uncontrolled bifurcation diagram in Fig. 12. As can be seen, even though this offset has been introduced, the uncontrolled system still stalls when the same persistent disturbances are introduced to the system. This point can be illustrated further by means of Fig. 22, which shows the system response to a persistent disturbance with the maximum offset in Fig. 19 added to K_{C9}. The same persistent disturbance introduced in the first disturbance scenario of Fig. 14 is once again introduced to the system. As can be seen, the system still enters rotating stall. This should provide definite evidence for the claim that the system is not simply being throttled to a previously stable equilibrium point by this controller. When the controller is on, the system simply does not enter rotating stall as it does in the scenario shown in Fig. 22.

In Fig. 23, the open and closed-loop bifurcation diagrams have been sketched with an estimated hypothetical stall inception point and compared to experimental data. This point was estimated using the bifurcation diagrams to determine where the peak pressure rise Ψ occurs. The addition of this point to the bifurcation diagram emphasizes the effect that impulsive disturbances have on the effective or perceived stall inception point of the compressor, as discussed in Part 1 of this article. The controller has eliminated the hysteresis region by enlarging the domains of attraction of linearly stable axisymmetric equilibrium points. Thus, the effective stable flow range of the compressor has been extended.

VI. Conclusions

In this article, experimental validation of the simplified approach to control of rotating stall has been provided for a low-speed, single-stage axial compressor rig. It was shown that the controller based on this approach has significant ability to reject persistent disturbances that cause the uncontrolled system to enter rotating stall. In addition, it was shown that the effective stable axisymmetric flow range of the compressor has been extended by this controller, hence, the controller enlarged the domains of attraction of the linearly stable axisymmetric equilibria. The experimental behaviors presented in this article were qualitatively completely consistent with the behaviors described in Part 1 of this article. These results provide an indication that rotating stall can potentially be controlled and performance benefits can be obtained using a single one-dimensional axisymmetric effector with relatively low bandwidth. The presence of rotating stall precursors in this rig was also demonstrated. It was found that two first mode rotating stall precursors traveling at different speeds could be detected in this rig provided that appropriate filtering is performed on measured data. It was also found that rotating stall grows smoothly out of one of these precursors.

The validation of this rotating stall control approach in the context of a low-speed, single-stage axial rig that was performed in this article is a first step towards complete validation of the approach developed in Part 1 of this article. There are, however, a number of open research topics that may serve to extend the results in this article. These include 1) validation of the simplified control approach in the context of a low-speed multistage rig and high-speed compressor rigs and 2) evaluation of the effectiveness of this controller in the presence of more realistic disturbances such as inlet distortion. Such disturbances can be introduced with air injection ports[16] or by wiggling inlet guide vanes.[15]

Acknowledgments

This work was supported by ONR and NSF. The work of the third author was also supported by the Air Force Laboratory Graduate Fellowship Program.

References

[1]Badmus, O. O., Chowdhury, S., Eveker, K. M., Nett, C. N., and Rivera, C. J., "Simplified Approach for Control of Rotating Stall Part 1: Theoretical Development," *Journal of Propulsion and Power*, Vol. 11, No. 6, 1995, pp. 1195–1209.

[2]Nett, C. N., "LICCHUS Experimental Facilities Summary: September 1991 (Months 1–18), October 1991," Videotape Presentation, School of Aerospace Engineering, Georgia Inst. of Technology, At-

lanta, GA.

[3]Badmus, O. O., Chowdhury, S., Eveker, K. M., and Nett, C. N., "Control-Oriented High-Frequency Turbomachinery Modeling: Single-Stage Compression System 1D Model, 1993," American Society of Mechanical Engineers 93-GT-385, 1993; also *Journal of Turbomachinery* (to be published).

[4]Eveker, K. M., and Nett, C. N., "Control of Compression System Surge and Rotating Stall: A Laboratory-Based "Hands-On" Introduction," *Proceedings of the 1993 American Control Conference*, 1993.

[5]Eveker, K. M., and Nett, C. N., "Control of Compression System Surge and Rotating Stall: A Laboratory-Based "Hands-On" Introduction," *Video Proceedings of the 1993 American Control Conference*, Georgia Inst. of Technology, Atlanta, GA, 1993.

[6]Moore, F. K., and Greitzer, E. M., "A Theory of Post-Stall Transients in Axial Compression Systems: Part 1, Development of Equations and Part 2, Application," *Journal of Turbomachinery*, Vol. 108, 1986, pp. 68–76, 231–239.

[7]Thompson, J. W., and Abernathy, R. B., "Handbook of Uncertainty in Gas Turbine Measurements," Arnold Engineering Development Center, AEDC-TR-73-5, Feb. 1973.

[8]Oppenheim, A. V., Willsky, A. S., and Young, I. T., *Signals and Systems*, Prentice–Hall, Englewood Cliffs, NJ, 1983.

[9]McDougall, N. M., Cumpsty, N. A., and Hynes, T. P., "Stall Inception in Axial Compressors," *Transactions of the American Society of Mechanical Engineers*, Vol. 112, Jan. 1990, pp. 116–125.

[10]Garnier, V. H., Epstein, A. H., and Greitzer, E. M., "Rotating Waves as a Stall Inception Indication in Axial Compressors," *Journal of Turbomachinery*, Vol. 113, No. 2, 1991, pp. 290–302.

[11]Day, I. J., "Stall Inception in Axial Flow Compressors," *International Gas Turbine and Aeroengine Congress and Exposition*, American Society of Mechanical Engineers, 91-GT-86, June 1991.

[12]Epstein, A. H., Ffowcs-Williams, J. E., and Greitzer, E. M., "Active Suppression of Aerodynamic Instabilities in Turbomachines," *Journal of Propulsion and Power*, Vol. 5, No. 2, 1989, pp. 204–211.

[13]Dugundji, J., Garnier, V. H., Epstein, A. H., Greitzer, E. M., Guenette, G., Paduano, J., Silkowski, P., Simon, J., and Valavani, L., "A Progress Report on Active Control of Flow Instabilities: Rotating Stall Stabilization in Axial Compressors," *Proceedings of the 1989 AIAA 2nd Shear Flow Conference*, AIAA, Washington, DC, 1989 (AIAA Paper 89-1008).

[14]Lawless, P., and Fleeter, S., "Active Unsteady Aerodynamic Suppression of Rotating Stall in an Incompressible Flow Centrifugal Compressor with Vaned Diffuser," *AIAA/SAE/ASME/ASEE 27th Joint Propulsion Conference*, AIAA, Washington, DC, 1991 (AIAA Paper 91-1898).

[15]Paduano, J., "Active Control of Rotating Stall in Axial Compressors," Ph.D. Dissertation, Massachusetts Inst. of Technology, Cambridge, MA, 1991.

[16]Day, I. J., "Active Suppression of Rotating Stall and Surge in Axial Compressors," *International Gas Turbine and Aeroengine Congress and Exposition*, 1991 (91-GT-87).